analytical chemistry

Article

pubs.acs.org/ac

Contact-Free Scanning and Imaging with the Scanning Ion Conductance Microscope

Samantha Del Linz,[⊥,†] Eero Willman,[§,∥] Matthew Caldwell,[⊥,†,∥] David Klenerman,[‡] Anibal Fernández,[§] and Guy Moss*[,⊥,†]

[⊥]Department of Neuroscience, Physiology and Pharmacology, University College London, Gower Street, London WC1E 6BT, United Kingdom

[†]Centre for Mathematics and Physics in the Life Sciences and Experimental Biology, University College London, Gower Street, London WC1E 6BT, United Kingdom

[§]Department of Electronic and Electrical Engineering, University College London, Torrington Place, London WC1E 7JE, United Kingdom

[‡]Department of Chemistry, Cambridge University, Lensfield Road, Cambridge CB2 1EW, United Kingdom

Supporting Information

ABSTRACT: Scanning ion conductance microscopy (SICM) offers the ability to obtain very high-resolution topographical images of living cells. One of the great advantages of SICM lies in its ability to perform contact-free scanning. However, it is not yet clear when the requirements for this scan mode are met. We have used finite element modeling (FEM) to examine the conditions for contact-free scanning. Our findings provide a framework for understanding the contact-free mode of SICM and also extend previous findings with regard to SICM resolution. Finally, we demonstrate the importance of our findings for accurate biological imaging.

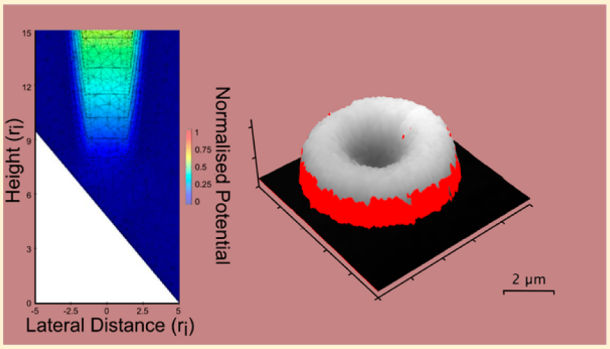

Scanning ion conductance microscopy (SICM) can provide very high-resolution topographical imaging without contacting the sample, a major advantage for biological imaging.[1,2] However, the precise requirements for contact-free scanning are currently unknown. Here, we address this issue using 3D finite element modeling (FEM). We show that FEM predictions agree closely with both theoretical calculations (in analytically tractable situations) and experimental measurements. Our results shed light on the conditions that are required to maintain contact-free scanning and extend previous work on SICM image formation and microscope resolution. Finally, by scanning red cells, we demonstrate the practical importance of these findings for accurate biological imaging.

MATERIALS AND METHODS

Scanning Ion Conductance Microscopy. SICM experiments were performed using an Ionscope scanning ion conductance microscope (Ionscope Ltd., Melbourn, U.K.), mounted on top of a Nikon TE2000 optical microscope (Nikon, Tokyo, Japan). Pipettes were pulled from borosilicate capillaries of 1.0 mm outside diameter (o.d.) × 0.50 mm inside diameter (i.d.) (Sutter Instrument, Novato, CA) using a P-2000 laser puller (Sutter Instrument). For measuring the approach to a flat surface and for the profile across a square step, probe total resistances (series + access; $R_s + R_a$) were 29 and 30 MΩ, respectively, whereas for the topographical imaging of erythrocytes, the probe resistance was 125 MΩ. All pipettes were filled with saline solution (140 mM NaCl, 4.7 mM KCl, 1.2 mM $MgCl_2$, 2.5 mM $CaCl_2$, 5 mM HEPES, 11 mM D-glucose, titrated to pH 7.4 with NaOH, (all reagents purchased from VWR International, Leicestershire, U.K.)), which also contained 20 μM Alexa Fluor 568 (Life Technologies, Paisley, U.K.) for measuring the approach to a flat surface and for the profile across a square step. The same saline solution (without fluorescent dye) was used in the bath for all the experiments. Scans were recorded using an applied potential in the range of 20−200 mV. Data were acquired in hopping mode using a range of set points from 0.3 to 1.0%. Optical images of pipettes were obtained using a Nikon 60×/0.85 NA objective and an Andor iXon3 888 EMCCD camera (Andor Technology, Belfast, U.K.). To examine the scan profile across a square step, PDMS casts of an AFM target (HS-500MG, Budget-Sensors, Innovative Solutions Bulgaria, Sofia, Bulgaria) were used. To examine changes in red cell images following changes in the scan set point, a small drop (∼ 50 μL) of blood was obtained by pin prick and diluted in 3 mL of saline solution. The erythrocytes were adhered to uncoated grade 0 glass

Received: August 29, 2013
Accepted: January 23, 2014
Published: February 12, 2014

   dx.doi.org/10.1021/ac402748j | Anal. Chem. 2014, 86, 2353−2360

coverslips (VWR) by incubating this solution for 10 min at room temperature. Samples were then washed three times in saline solution before SICM imaging. Scan images were rendered and analyzed using "Ionview", in-house software written for Mac OS X and available at http://walkytalky.net/ionview/.

Modeling Approach. Solutions for the electric potential distribution over the entire three-dimensional geometry were sought using a variational approach implemented by the finite element method. The current density was then found from the potential distribution.

The finite element method requires that the volume be divided into a mesh of small elements. For this, we used the commercial mesh generation program GiD (http://gid.cimne.upc.es/) driven by a batch file created in MATLAB (The MathWorks, Natick, MA). Unstructured meshes of tetrahedral elements were generated, with elements of variable size. Fine meshing was used in regions such as that around the pipet tip, where rapid changes in potential can occur. Mesh size was varied to confirm that the solutions were not mesh-dependent. For example, the maximum spacing of mesh elements in the finer regions was varied between 0.01−0.2 units with no observed change in solution. The simulation volume was also varied to ensure that solutions in larger volumes were, again, identical within expected error margins. Units of distance were expressed in multiples of the pipet inner radius (r_i) such that results were independent of an assumed pipet size.

The potential distribution φ was found by seeking a stationary solution to the following variational functional J, a quantity proportional to the stored electric energy and derived from the Laplace equation:

$$J = \int_V (\nabla\varphi)\,(\varepsilon\nabla\varphi \mathrm{dV}) \tag{1}$$

where dV is the differential volume , and ε is the permittivity. The finite element program and the visualization program were adapted from in-house software designed for liquid crystal modeling in the Department of Electronic and Electrical Engineering, UCL, London, U.K. (http://www.ee.ucl.ac.uk/LCmodelling).

The wire electrode inside the pipet was simulated as a disc positioned at a fixed distance from the pipet mouth where a Dirichlet boundary condition was imposed (i.e., a fixed potential $\varphi = \varphi_o$ was assigned to it). The ground electrode was simulated as a ring around the perimeter of the simulation volume to allow a smaller total simulation volume to be used and to avoid biasing any particular direction. The ground electrode was given the fixed potential of 0. The walls of the pipet were treated as a dielectric with the permittivity of borosilicate glass of (4.7 ε_0, where ε_0 is the permittivity of free space). The inside of the pipet and the bath were treated as a conducting solution of conductivity 1.25 Ω^{-1} m^{-1} (calculated as the inverse of the resistivity of Ringer's solution[3] of 80 Ω·cm, or occasionally of conductivity 1.56 Ω^{-1} m^{-1} (for comparison with experimental data obtained using a solution of resistivity 64 Ω·cm). At the dielectric-liquid boundaries, the rate of change of φ with respect to the surface normal n, $\partial\varphi/\partial$n, was allowed to be discontinuous, setting it to zero on the liquid side and leaving it free on the dielectric side to satisfy the correct boundary condition for the current.

The current density $\vec{J}$ flowing through the pipet was then calculated from the electric potential as: $\vec{J} = \sigma\nabla\varphi$ where σ is the electric conductivity of the solution. The total current arriving at a surface was then found as the integral of the normal component of the current density. In our calculations, we only include the tip of the pipet in the simulation volume and not its entire length, so the pipet series resistance (R_s) was adjusted to compensate for the truncated pipet length used, and the current was rescaled based on this new resistance.

Except where noted, our simulations employed a half-cone angle of 3° (Figure 1B), an angle consistent with estimates for SICM pipettes made by Ying et al. using electron microscopy.[4] Further, most simulations were restricted to capillary glass

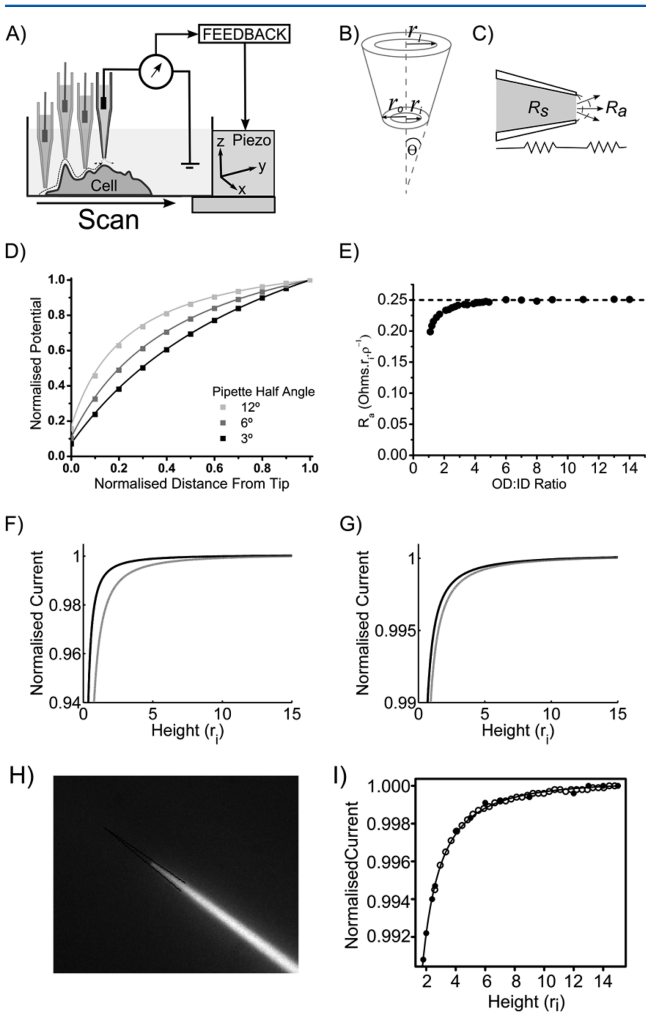

Figure 1. SICM simulations agree with theory and experiment. (A) Schematic showing the principle of SICM imaging. (B) Important SICM parameters are the probe tip's inner and outer radii, r_i and r_o, and the half-cone angle θ. The inner radius at the wide end, $r_{i,}$ is $\gg r_i$ and can be neglected in many calculations. (C) Schematic of series resistance R_s and access resistance R_a. (D) The potential drop inside the probe calculated by FEM (solid markers) and analytically (solid lines). (E) FEM calculations of access resistance (solid markers) and the value predicted analytically for a circular pore in an infinite plane (dotted line[9]). (F) Approach curve simulations for half-cone angles of 3° (black line) and 9° (gray line), both with i.d./o.d. ratio of 0.58. (G) Approach curve simulations for glass i.d./o.d. ratios of 0.78 (black line) and 0.5 (gray line), both with half-cone angle of 1.8°. (H) Image of the pipet used to measure approach curves. Tip radius was determined from the half-cone angle using eq 5. (I) Experimental data (open circles, average of 67 approach curves) and predicted approach curve (solid line) from simulated data (solid circles). The x-axis was rescaled in units of r_i (measured as 166 nm).

dx.doi.org/10.1021/ac402748j | Anal. Chem. 2014, 86, 2353−2360

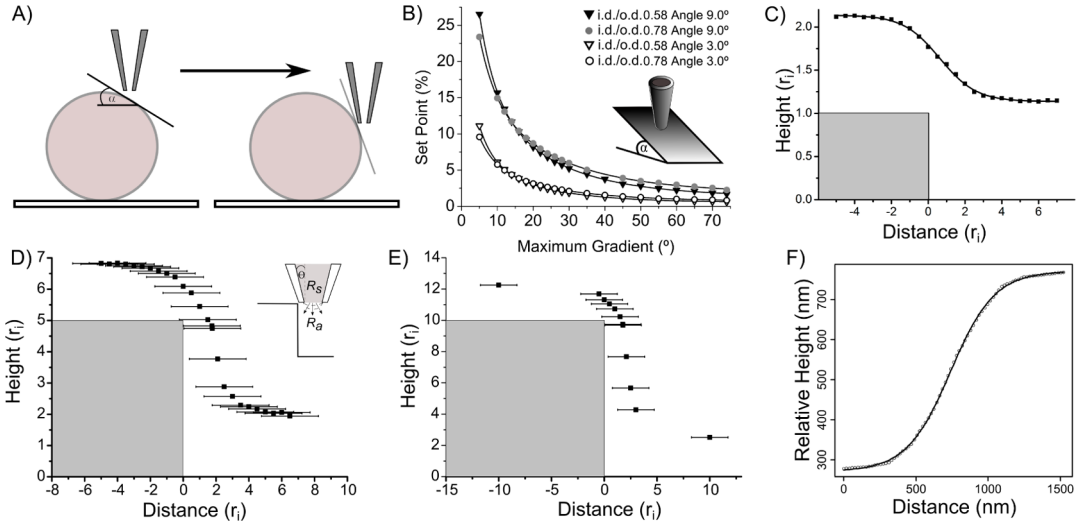

Figure 2. Ability of SICM to maintain contact-free scanning. (A) Schematic illustrating the difficulty in scanning a cell surface as the slope (α) varies. (B) FEM simulations of the pipet approaching a planar surface (slope α, inset). The highest contact-free gradient for each set point is plotted for two half-cone angles and two glass i.d./o.d. ratios. (C) Scan over a square step of $1r_i$ (1% set point) with the profile fit to eq 6. (D) Scan over $5r_i$ and $10r_i$ (E) steps (i.d./o.d. ratio of 0.58) at set points of 0.5% and 0.4%. The solid line fit in (C) is to eq 6. Bars in the x-direction indicate the outer edges of the pipet tip. (F) Experimental scan of a 500 nm square step with solid line fit to eq 6.

o.d./i.d. ratios that represent commercially available capillaries likely to be used in SICM experiments (i.e., ratios of ~1.28 to 2.0). We assumed these ratios were unchanged during probe manufacture.[5] The major exception to this was in simulations to examine the probe access resistance, where o.d./i.d. ratios of 1.1−15 were simulated.

All approach curve simulations were carried out by first calculating the electric potential at fixed probe positions and then calculating the current flow at each of these positions. SICM does not operate by measuring current at fixed positions but instead uses a fixed current reduction (the set point current) to estimate the specimen height (Figure 1A). Therefore, in order to extract height predictions from the discrete simulated approach curves, the data were fitted to a continuous function (Figure S-1 in the Supporting Information) of the following form:

$$I = \frac{1}{A_1 + \frac{A_2}{Z^{A_3}} + \frac{A_4}{Z^{A_5}}} \tag{2}$$

Where I is the normalized pipet current (i.e., normalized to the current flow when the pipet is far from the surface), A_1 to A_5 are constants, and z is the height of the probe above the surface. We found empirically that for most surface geometries a curve of this form is able to fit the data without showing any systematic deviation in the residuals. Indeed in simple cases, for example the approach to a flat surface, the term containing A_4 and A_5 was not needed and was set to zero. However, in a very few cases, complex surface geometries produced fits that showed systematic deviations, even when all terms were allowed to vary and thus could not be relied upon for set point calculations. For these approach curves, we changed our procedure to fit this function only to a fraction of the full approach curve data such that the remaining residuals again showed no trend. These fits to the first part of the approach curve data were always sufficient to extract the requisite height at the set points analyzed, without extrapolation.

RESULTS

FEM Accurately Predicts Series Resistance, Access Resistance, and the Approach Curve to a Flat Surface. SICM probe sensitivity to the sample surface is determined by the ratio of probe series resistance (the resistance to ion flow inside the probe capillary) to probe access resistance (the resistance along all the convergent paths from the bulk medium to the mouth of the pipet)[6] (Figure 1C). We therefore began by testing our FEM calculations for these key resistances in a simple situation, where the probe does not interact with a surface. In this condition, both access resistance and series resistance can be calculated analytically. Series resistance causes a drop of potential along the shaft of the probe which is easily calculated[4,7,8] (Figure S-2) as:

$$\varphi(z) = \varphi_o\left(\frac{R(Z) + R_a}{R_s + R_a}\right) \tag{3}$$

where $\varphi(z)$ is the potential at vertical position z (between the tip and wire electrode), φ_o is the potential of the wire electrode inside the probe, R_s is the series resistance of the entire probe between the internal wire and tip, R_a is the probe access resistance, and $R(z)$ is the resistance of the pipet from the tip to position z (Figure S-2). $R(z)$ is given by:

$$R(z) = \frac{\rho}{\pi \tan(\theta)}\left(\frac{1}{r_i} - \frac{1}{r_i + z\tan(\theta)}\right) \tag{4}$$

where ρ is the resistivity of the solution filling the probe, r_i is the inner radius at the probe tip, and θ is the pipet half-cone angle. For this resistance, FEM simulations agree nearly perfectly with the analytical solution (Figure 1D). We next examined probe access resistance. Access resistance will vary with the glass o.d./i.d. ratio. We therefore calculated this resistance over a range of capillary dimensions (Figure 1E). We found that in open solution, the access resistance varies by only ~10% over o.d./i.d. glass ratios that are likely to be of interest to experimenters (ratios of ~1.28−2.0). Furthermore, the value of access resistance plateaus beyond glass o.d./i.d. values of ~5

dx.doi.org/10.1021/ac402748j | Anal. Chem. 2014, 86, 2353−2360

and can be compared to the analytical value calculated for a small circular pore in an infinite plane[9] (Figure 1E, dotted line). Agreement between our simulations and the analytical solution is excellent.

Approach Curve to a Flat Surface. Series and access resistance both affect the SICM approach curve to a flat surface (Figure 1F,G). Thus, as a further test of our FEM work, we simulated this type of approach curve and compared our results to those obtained experimentally. For experiments, we determined the pipet half-cone angle and inner radius by using comparatively large diameter pipettes filled with fluorescent dye so that they could be imaged optically (Figure 1I, inset). We also measured the resistivity of our pipet solution and the combined access resistance and pipet resistance when the pipet was far from the surface. Using Hall's solution to approximate access resistance[9] and simplifying eq 4 at large z, the inner pipet radius can be calculated using the half-cone angle, solution resistivity, and combined resistance (Supporting Material) as:

$$r_i = \frac{\rho}{R_s + R_a}\left(\frac{1}{\pi \tan(\theta)} + \frac{1}{4}\right) \quad (5)$$

The comparison of experimentally measured and simulated approach curves to a flat surface is shown in Figure 1I. To compare the two data sets, we fitted our simulated approach curve to a simplified version of eq 2 (setting A_4 and A_5 to zero). We then superimposed this curve, the simulated data, and our experimental data (recalibrating distances by the radius of the pipet used in our experiments, Figure 1H). Because both the half-cone angle and probe radius are measured experimentally, and we know the glass o.d./i.d. ratio, this makes for an exact comparison between simulation and experiment and allows no free parameters. As can be seen from Figure 1I, experiment agrees very well with simulation. Having validated our approach, we went on to examine the requirements for contact-free scanning.

Conditions for Contact-Free Scanning. Contact-free scanning is a challenge for biological imaging, because at the edge of cells, the slope can become very high, essentially vertical (Figure 2A). We therefore simulated the pipet approaching an angled planar surface (Figure 2B, inset) and then examined the maximum slope that can be scanned without contact at a given scan set point. Figure 2B shows summary data for two glass o.d./i.d. ratios and two different half-cone angles (3° and 9°). Taking a 2.5% set point as an example, the maximum slope that can be scanned with a probe half-cone angle of 3° is approximately 22°, whereas a half-cone angle of 9° allows slopes of ~53−69° (depending on the glass o.d./i.d. ratio). Thus, probe series resistance can have a major impact on the ability to scan slopes. As is also evident from these numbers, thinner glass is helpful at low set points, because it allows the probe to get closer to a sloping surface and the associated reduction in access resistance (and hence the loss of probe sensitivity) is less important than the change in geometry.

Interestingly, although the pipet half-cone angle limits the steepest planar slopes that can be simulated (Figure 2B, inset), it is clear that the curves of Figure 2B become increasingly shallow as the set point is decreased, suggesting that it is possible to scan over a 90° step without contact.

Scanning a Vertical Step. We simulated a range of steps that were larger than the pipet radius in both the x direction (width = $50r_i$) and the y direction (breadth =$30r_i$). Figure 2C−E shows simulations for steps of this type of height $1r_i$, $5r_i$, and $10r_i$. These steps can be scanned without contact, but larger steps require lower set points. Thus, a step $1r_i$ high is comfortably scanned at a 1% set point (Figure 2C), although at $5r_i$ and $10r_i$, the maximum contact-free set points are ~0.5% and ~0.4%, respectively. Because most reports in the literature use set points in the range of 1.0−0.4%, a step of $10r_i$ provides an upper estimate of the vertical drop that could be scanned contact-free in these experiments. Of course the absolute figure depends on the precise sensitivity and geometry of the probe (Figure 2B). Caldwell et al. introduced a calibration technique for measuring SICM probe tip radius and half-cone angle in nanopipettes and estimated half-cone angles of ~2° or less.[10] For this value, our data can be used to calculate that a set point of just ~0.2% (depending on glass thickness) would be needed to ensure contact-free scanning over a step of $10r_i$ (Figure S-3). Set points of 0.2% are below the limit of those currently reported for scanning and represent a considerable technical challenge. Thus, given current probe technology, $10r_i$ seems to be a reasonable upper estimate for the ability to scan contact-free at a vertical face.

We next compared our simulations to experiment. In order to make this comparison, we fitted the SICM step profiles predicted from simulations to a logistic function of the following form:

$$z = b_1 + \frac{b_2 - b_1}{1 + 10^{(X_{1/2} - x)p}} \quad (6)$$

where b_1, b_2, $X_{1/2}$, and p are constants, and x is the lateral distance. This equation fitted the simulated data reasonably well at our chosen set points and thus provided a useful comparison with the general form of the profile obtained from comparable experiments. Further, by fitting this equation (Figure 2C), we were able to quantify the lateral response by the distance required for a probe to go from 25% to 75% of the maximal step response. For a step $1r_i$ in height, the 25−75% response required $2.2 \pm 0.1r_i$ (1% set point), and for steps of height $5r_i$, (0.5% set point) and $10r_i$ (0.4% set point), the values obtained were $1.8 \pm 0.2r_i$ and $2.3 \pm 0.1r_i$, respectively. To attempt to make a suitable experimental comparison, we scanned a 500 nm square step calibration target (see Methods) using a 1% set point (Figure 2F). We then examined the scan profile at right angles to the step and fitted it to eq 6. The fit is very good, demonstrating that at this set point, the general form of the profile is very similar to that predicted by simulation. Further, assuming the experimentally measured 25−75% response is $\sim 2r_i$, then this predicts a pipet inner radius of 166 ± 2 nm. By using a large pipet filled with dye as described earlier, we could independently estimate the tip radius. The figure obtained was 161 ± 16 nm, so there is again both qualitative and quantitative agreement between theory and experiment.

Image Resolution. For tall objects, the requirement to scan contact-free will affect the choice of set point and this, in turn, will affect image resolution. In previous estimates of resolution, relatively small (low) objects have been examined of height $\leq 1r_i$. We therefore extended our simulations to look at the implications of contact-free scanning for image resolution, defining resolution as the ability to separate two nearby objects. Because these objects have finite width, we defined their separation by the distance between the closest edges of the objects at their nearest points. We considered the objects as being resolved when the "dip" in height between them was $\geq 0.05r_i$. (The z resolution of SICM is excellent but depends on

dx.doi.org/10.1021/ac402748j | Anal. Chem. 2014, 86, 2353−2360

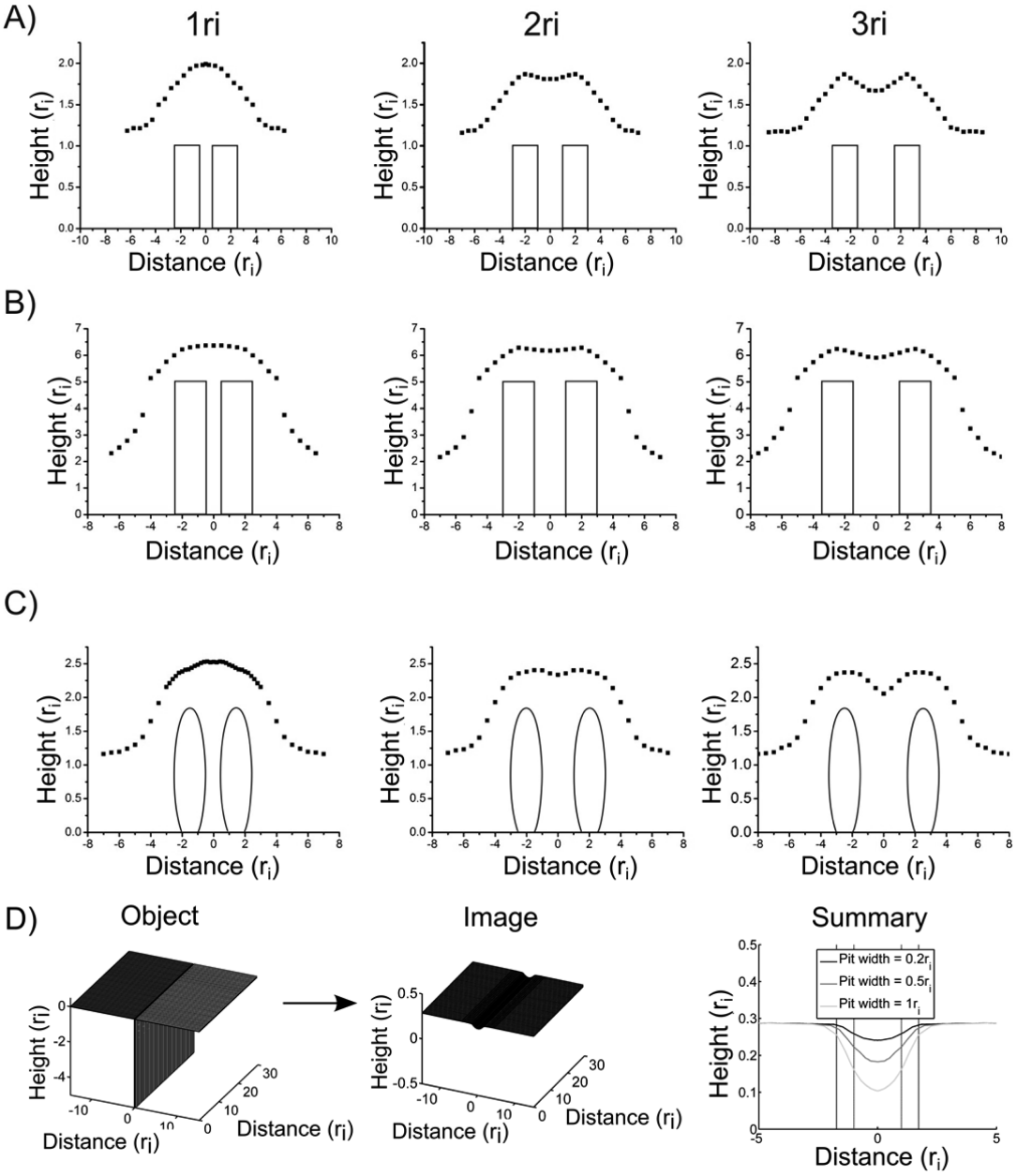

Figure 3. Contact-free scanning is consistent with a resolution of ~$2r_i$. (A) Scan profiles (filled squares, 1% set point) calculated across two square steps of height 1r_i, separated by1r_i, 2r_i, or 3r_i. (A cross-sectional view is shown.) (B) Profiles as in (A) but for a step 5r_i high and a set point of 0.49% (filled squares). (C) Scan profiles (filled squares,1% set point) as in (A) but for cylinders 1.85r_i tall. Spacing refers to the inner edges of these objects. (D) Simulated groove of depth 5r_i and width 0.2r_i (left panel) shown with the resulting image (at 5% set point, middle panel). The right-hand panel shows a summary of simulated profiles for grooves of different widths with vertical dashed and dotted lines indicating pipet inner and outer radii as measured from zero.

many factors that generate electrical noise in the system. If a typical SICM pipet is assumed to be of radius ~100 nm, a vertical resolution of ~5 nm (0.05r_i) is probably close to the limit of what is readily achievable in routine scans).

We began by examining elongated square steps of height 5r_i and, for comparison,1r_i. Our results are shown in Figure 3A,B. Objects of height 1r_i (scanned at a 1% set point) appear as a single peak at separations of 0.5−1.0r_i. However, at a separation of 2r_i the "dip" between objects is 0.07r_i, whereas at 3r_i, it is 0.2r_i. Thus, defining resolution as a "dip" of 0.05r_i or greater, objects of height 1r_i would just be resolvable at separations of approximately 2r_i when using a 1% set point. The taller objects (5r_i high) must be scanned at a reduced set point, and we simulated 0.49%. Importantly, we found that the effect of a reduced set point is compensated for by taller objects and again they were separable at ~2r_i (Figure 3B).

We next simulated scans across a pair of horizontal cylinder-like structures with an omega profile (Figure 3C), because in many biological samples, it is the separation of fine, horizontal "cylinders", such as nearby axons and dendrites, that is important in terms of resolution. Our objects had omega profiles of height 1.85r_i and width 2r_i. We again calculated image profiles at a 1% set point where contact-free scanning is possible. Interestingly, these objects were also just separable at a distance of approximately 2r_i (Figure 3C), with the dip between objects being 0.05r_i. Thus, by many measures, a

dx.doi.org/10.1021/ac402748j | Anal. Chem. 2014, 86, 2353−2360

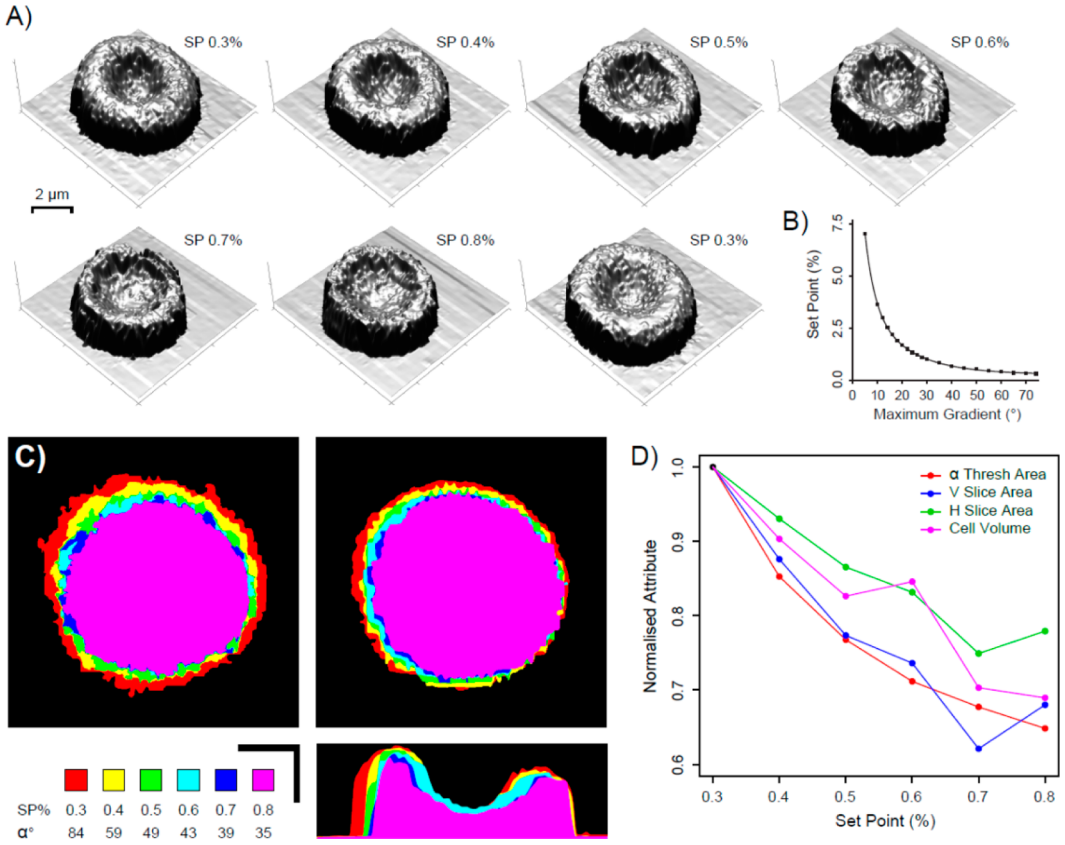

Figure 4. Impact of set point slope detection threshold when scanning biological samples. (A) Time series of scans of the same red blood cell at different set points (SP) from 0.3% to 0.8%, returning to a 0.3% set point in the final scan. (B) Variation of maximum scan gradient [α] with set point, as predicted by FEM for a pipet of the geometry used for imaging in (A). (C) Left: regions of the initial 0.3% scan whose gradient is within the detection threshold for different set points, as indicated in the key. Gradients within the interior hollow region are excluded for simplicity. Right: horizontal and vertical cross sections through the actual scans obtained at each set point show a similar reduction. Scale bars: 2 μm. (D) Comparison of the changes in cell geometry (horizontal slice area, vertical slice area, and volume) at set points seen in panels (A) and (C). All changes are normalized to the initial value at 0.3%.

resolution estimate of $2r_i$ seems realistic for SICM, even when maintaining contact-free scanning. However, it is important to keep in mind that if a lower set point is needed to avoid contact with taller features, then the resolution of smaller objects is not as good (Figure S-4).

As a final test of SICM resolution, we investigated scanning over narrow square grooves, where the separation is smaller than, or comparable to, the pipet radius. We simulated grooves of width $\leq 1r_i$ but of length $\gg 3r_i$ and depth $5r_i$. We found that these features would be hard to detect at a 1% set point, so we calculated image profiles using an increased set point of 5%, which again can be done contact-free for this particular target geometry. The results from the simulations are shown in Figure 3D. Narrow separations between objects can be detected and appear broadened and rounded in the SICM image such that their width appears to be $\sim 2r_i$, regardless of their underlying feature width (in the range $0.2r_i - 1r_i$). In other words, these features become broadened by convolution with what is effectively a rounded point spread function of the probe. Further, when the grooves are made deeper, progressively smaller increases in apparent depth appear in the image, so depth fidelity is poor (data not shown). Looking at these narrow separations as another measure of image resolution, we can see that SICM detection can be very good, although image fidelity is poor and caution must be exercised when interpreting such images.

Red Cell Images Illustrate the Framework for Contact-Free Scanning. We next examined the practical implications of our simulations by imaging red cells at a variety of set points. To compare experiment with theory, we first scanned at a very low set point (0.3%, Figure 4A, first image), producing an estimate of the true topography of the upper surface. The images at this set point show parameters that are those of a typical red cell as measured by other techniques,[11] with a width of ~7.7 μm and a volume of ~96 fl. (It should be noted, however, that SICM, like other scanning probe techniques, cannot visualize the underneath side of protruding objects. For this reason, the very edges of cells can appear, as in this case, to be vertical.) We then used our simulation results (Figure 4B) and the 0.3% scan image to identify regions of the cell where we would expect collisions to occur at set points above 0.3% (specifically, 0.4, 0.5, 0.6, 0.7, 0.8, and 0.9%), Figure 4C (upper left panel). (Note there is a slight asymmetry in the predicted areas of collision, because the imaged cell is not lying entirely flat on its substrate.) We then scanned the cell at these set points, finally returning to a scan using a 0.3% set point to make sure that apparent changes in the cell geometry were the result of probe contact rather than an unprompted series of movements by the cell in these regions. The scans are shown in Figure 4A. As the set point is increased, the maximum slope the scan can cope with decreases. At the edge of the cell, where the steepest angles occur, the apparent changes in cell radius

dx.doi.org/10.1021/ac402748j | Anal. Chem. 2014, 86, 2353−2360

match the predicted regions of collision closely (Figure 4C). When the set point is returned to 0.3%, the cell image is restored. Thus, the effect of not operating in contact-free conditions is to give a false impression of improved resolution and to produce large changes in apparent cell volume and area, all showing a trend that can be anticipated by examining the slopes of the sample in relation to the pipet geometry and set point (Figure 4C, D).

DISCUSSION

A number of reports have used finite element analysis to understand the behavior of the SICM-like probes,[6,7,12,13] but contact-free scanning has not been examined to date. This is particularly important for biological imaging, because cell responses to contact (e.g., via the mechano-sensitive ion channels) are widely prevalent, playing central roles in regulating cell volume and function.[13] Indeed, when imaging cellular dynamics, provided that the images have the necessary resolution to identify the structures of interest, the ability to maintain contact-free scanning (and thereby to avoid interactions with the sample) may well be more important than the precise determination of feature sizes.

We have found that the ratio of access to series resistance plays a critical role in contact-free scanning. Also important is the o.d./i.d. ratio of the glass, which limits the probe's physical access to a sloping surface. For low set points, substantially higher slopes can be scanned contact-free with a low o.d./i.d. ratio. This is because for experimentally realistic parameter values, the influence of glass thickness in changing the critical ratio between probe access and series resistance is limited at these set points.

We also investigated the implications of contact-free scanning for SICM resolution. For small steps ($1r_i$ high), that are simple to scan contact-free, Edwards et al. have previously pointed out that the total influence of the pipet, convolved with the step (i.e., the 0−100% response of the pipet) was apparent over approximately four tip radii.[6] Their result, for a low step, is thus in good agreement with our figure for the 25−75% response ($\sim 2r_i$) for both small and large steps. In another study, Rheinlaender and Schäffer[7] looked at the ability to separate two nearby vertical cylinders of height $1r_i$ or less. They defined the lateral resolution as the point at which a "dip" between objects vanishes making them inseparable, regardless of the set point. They found that this occurred at a separation of $3r_i$ which was defined by the distance between object centers. These objects were $1r_i$ in diameter, so this equates to inner edges separated by $2r_i$. If this result could be generalized to any geometry, it would be theoretically impossible to distinguish the objects shown in Figure 4. Thus, one advance that emerges from our simulations is that resolution depends on the object geometry. For the objects we considered, the dip does not vanish at a separation of $2r_i$, and indeed, it is likely to be experimentally observable with realistic pipet geometries. This is true even at $1r_i$ high and probably results from the reduced interactions of height and width for our steps versus the cylinders considered by Rheinlaender and Schäffer (Figure S-5). When taller objects are scanned, lower set points are needed, but the resolution of tall objects is $\sim 2r_i$. However, there is a loss of resolution for small objects. Further, to visualize either tall or large features as completely separate objects would, of course, require a much larger separation, $\sim 6-10r_i$.[7] (Alternatively, it may be possible to use deconvolution techniques to recover an image of separate objects in simple cases (see, for example, the point spread function approach of Rheinlaender and Schäffer[7]). Nonetheless, interactions between x, y, and z geometry discussed above make it much more difficult (perhaps impossible) to find unique solutions in more complicated cases.) Importantly, for biological imaging, having a set point that is too high can give an artificial impression of high resolution, probably because recently discovered intrinsic forces maintain pipet−membrane separation and substantially distort the cell.[15] (Of course, contact-free scanning is necessary, not sufficient to ensure force-free scanning.[15,16]) Finally, in a special case, our results show that a separation between objects in the form of a very narrow groove can appear as a detectable dip at high set points even for a groove of $0.2r_i$.

Clearly the interaction between contact-free scan conditions (via set point) and image resolution is important. In the future, it should be possible to use information about the conditions for contact-free scanning to optimize resolution and thus to create better scan protocols. For example, following a preliminary contact-free scan using a very low set point, the slopes and heights in the image can be analyzed to identify regions where it is possible to scan contact-free at higher set points and hence to obtain better resolution in these regions while still operating in contact-free mode.

CONCLUSION

We have examined the conditions for contact-free SICM imaging, characterizing the range of slopes and probe set points for which it is possible to scan contact-free. We have also shown it is possible to scan over a vertical step, provided its height is less than ∼10 times the internal radius of the pipet. For taller objects, or when using higher set points, contact-free scanning is likely to become technically difficult given the geometry of pipettes currently in use as reported in the literature.

We have also found that the precise resolution of SICM depends on the geometry of the objects being imaged. We estimate that for many biological samples, imaged under experimentally realistic conditions, objects separated by $\sim 2r_i$ will be resolvable. Finally, we have demonstrated the importance of contact-free scanning for accurate biological imaging in relation to feature size and volume. These findings should thus aid the development of scan protocols designed to obtain the optimal combination of contact-free scanning and image resolution in the future.

ASSOCIATED CONTENT

Supporting Information

Additional information as noted in the text. This material is available free of charge via the Internet at http://pubs.acs.org.

AUTHOR INFORMATION

Corresponding Author

*E-mail: g.moss@ucl.ac.uk.

Author Contributions

‖These authors contributed equally.

Notes

The authors declare the following competing financial interest(s): D.K. is a shareholder in Ionscope Ltd, who sell SICM systems, and he is also a consultant to the company. G.M. and A.F. have a CASE studentship award supported by Ionscope Ltd.

■ ACKNOWLEDGMENTS

This work was supported by the Biotechnology and Biological Sciences Research Council and by the Engineering and Physical Sciences Research Council. We thank Adam Orchard and Guillaume Charras for PDMS casting.

■ REFERENCES

(1) Hansma, P. K.; Drake, B.; Marti, O.; Gould, S. A.; Prater, C. B. *Science* **1989**, *243*, 641−643.
(2) Korchev, Y. E.; Bashford, C. L.; Milovanovic, M.; Vodyanoy, I.; Lab, M. J. *Biophys. J.* **1997**, *73*, 653−658.
(3) Hille, B. *Ionic Channels of Excitable Membranes*; Sinauer Associates, Inc.: Sunderland, MA, 1984; p 8.
(4) Ying, L.; White, S. S.; Bruckbauer, A.; Meadows, L.; Korchev, Y. E; Klenerman, D. *Biophys. J.* **2004**, *86*, 1018−1027.
(5) Corey, D. P.; Stevens, C. F. In *Single Channel Recording*; Sakmann, B., Neher, E., Eds.; Plenum Press: New York, 1983; pp 53−68.
(6) Edwards, M. A.; Williams, C. G.; Whitworth, A. L.; Unwin, P. R. *Anal. Chem.* **2009**, *81*, 4482−4492.
(7) Rheinlaender, J.; Schäffer, T. E. *J. Appl. Phys.* **2009**, 105.
(8) Snell, F. M. In *Glass Microelectrodes*; Lavallée, M., Schanne, O. F., Hébert, N. C. , Eds.; Wiley: New York, 1969; pp 111−123.
(9) Hall, J. E. *J. Gen. Physiol.* **1975**, *66*, 531−532.
(10) Caldwell, M.; Del Linz, S. J. L.; Smart, T. G.; Moss, G. W. J. *Anal. Chem.* **2012**, *84*, 8980−8984.
(11) Tomaiuolo, G.; Rossi, D.; Caserta, S.; Cesarelli, M.; Guido, S. *Cytometry, Part A* **2012**, *81*, 1040−1047.
(12) Bae, C.; Butler, P. J. *Biomech. Model. Mechanobiol.* **2008**, *7*, 379−386.
(13) Chen, C. C.; Baker, L. A. *Analyst* **2011**, *136*, 90−97.
(14) Sachs, F. *Physiology* **2010**, *25*, 50−56.
(15) Clarke, R. W.; Zhukov, A.; Richards, O.; Johnson, N.; Ostanin, V.; Klenerman, D. *J. Am. Chem. Soc.* **2013**, *135*, 322−329.
(16) Pellegrino, M.; Orsini, P.; Pellegrini, M.; Baschieri, P.; Dinelli, F.; Petracchi, D.; Tognoni, E.; Ascoli, C. *Neurosci. Res.* **2011**, *69*, 234−240.